East European Journal of Physics. 1. 60–75 (2026)
DOI: 10.26565/2312-4334-2026-1-05 ISSN 2312-4334

COSMOLOGICAL DIAGNOSTICS OF BIANCHI TYPE-*II* BARROW HOLOGRAPHIC DARK ENERGY UNIVERSE

U.Y. Divya Prasanthi[1], **D. Tejeswararao**[2,*], **Diddi Srinivasa Rao**[3], **Y. Aditya**[4,*], **D. Ram Babu**[4]
[1]*Department of Statistics & Mathematics, College of Horticulture, Dr. Y.S.R. Horticultural University, Parvathipuram-535502, India*
[2]*Department of Basic Sciences and Humanities, GMR Institute of Technology (GMRIT) – Deemed to be University, Rajam-532127, India*
[3]*Department of Mathematics, Aditya University, Surampalem-533437, India*
[4]*Department of Mathematics, GMR Institute of Technology (GMRIT) – Deemed to be University, Rajam-532127, India*
[*]*Corresponding Author e-mail: yaditya2@gmail.com; aditya.y@gmail.com*
[*]*Corresponding Author e-mail: teja.iict@gmail.com*
Received September 26, 2025; revised January 2, 2026; in final form January 27, 2026; accepted January 29, 2026

In this paper, we investigate a Bianchi type-*II* anisotropic cosmological model in the framework of Barrow holographic dark energy, considering both the Hubble horizon and Granda–Oliveros scale as infrared cutoffs. To obtain exact solutions of the Einstein field equations, we assume a suitable relation between the metric potentials. Using Hubble cosmic chronometer data, we constrain the model parameters and obtain the best-fit values $b_4 = -0.091^{+0.013}_{-0.012}$ and $H_0 = 72.3 \pm 2.7$ km s^{-1}Mpc^{-1}. The $H(z)$ fit shows excellent agreement with observational data and overlaps with ΛCDM at low redshifts, with mild deviations at higher z. The physical behaviour of the model is examined through a detailed analysis of cosmological parameters. The deceleration parameter $q(z)$ reveals a smooth transition from an early decelerating phase to the present accelerating epoch. The equation of state parameter ω_{de} shows quintom-like dynamics, evolving across the cosmological constant boundary and entering the phantom regime, consistent with late-time acceleration. Stability is tested using the squared sound speed v_s^2, which remains positive in the recent Universe, ensuring classical stability. The $\omega_{de} - \omega'_{de}$ phase plane indicates that both models lie in the freezing region, corresponding to faster acceleration. The statefinder diagnostics (r, s) and (r, q) further confirm the transition from the standard cold dark matter dominated phase to a de Sitter-like attractor, with trajectories showing clear deviations from ΛCDM.

Keywords: *Bianchi type-II model; Barrow holographic dark energy; Dark energy; Cosmology; Modified theory of gravity*

PACS: 98.80.-k, 04.50.+h, 95.30.Sf

1. INTRODUCTION

One of the most fascinating topics in theoretical and experimental cosmology is the enigma of dark energy (DE), feature of the universe that propels cosmic acceleration [1]-[3]. Among the more attractive DE model candidates put forth in the literature is the holographic DE (HDE) idea. The origin of the connection between a quantum theory's IR cut-off and ultraviolet cut-off, which is the greatest distance at a cosmological scale, is the holographic principle [4, 5]. This principle states that the two-dimensional bounding area of the universe horizon entropy is similar to the Benkenstein-Hawking law of Black hole entropy area. The age of cosmic acceleration could not be described by the initial HDE model, which was proposed with the Hubble horizon as the IR cut-off [6]. To achieve this, physicists made various assumptions about horizon entropy and IR cut-off sizes, which resulted in a number of distinct HDE modes. A different DE model that exhibits a time-varying dynamic equation of state (EoS) and is in accordance with the quantum principle that obeys the Heisenberg type uncertainty principle is the HDE model. In issues that described the inflationary era and the bounce scenario, HDE models also saw significant success. Over recent decades, various entropy formulations have been applied to develop and examine cosmological models. This has led to several innovative HDE models, such as the Tsallis HDE [7, 8], Sharma-Mittal HDE (SMHDE) [9], and Renyi HDE model [10]. Numerous researchers have evaluated cosmological models based on these new HDE concepts [11] - [21]. Recently, Kaniadakis statistics have been utilized as a generalized measure of entropy [22] - [24] to investigate various gravitational and cosmological phenomena. Kaniadakis entropy modifies the standard thermodynamics, allowing for non-linearities that account for a broader range of behaviors in DE. It provides a more generalized EoS, enabling flexibility in describing the evolution of DE over cosmic time. Barrow [25] introduced a generalized entropy–area relation that accounts for quantum gravitational effects through a fractal deformation of the horizon surface. This leads to the concept of Barrow entropy, characterized by the deformation parameter δ, which quantifies deviations from the standard entropy law. When applied to the holographic framework, this correction yields the Barrow HDE (BHDE) model. The inclusion of Barrow entropy enriches the thermodynamic foundation of DE, linking quantum gravitational effects with cosmic expansion and offering a broader understanding of the universe's late-time acceleration. It should be noted that in [26, 27], cosmological limitations on parameter δ have been inferred. Oliveros et al. [28] studied the BHDE model using the Granda–Oliveros IR cutoff and provided a detailed account

Cite as: U.Y.D. Prasanthi, D. Tejeswararao, Diddi Srinivasa Rao, Y. Aditya, D. Ram Babu, East Eur. J. Phys. 1, 60 (2026), https://doi.org/10.26565/2312-4334-2026-1-05

of its cosmic evolution. Remya et al. [29] analyzed the cosmological behavior of BHDE incorporating a time-varying deceleration parameter, while Koussour et al. [30] explored the BT-I spacetime influenced by BHDE using the Hubble horizon as the IR cutoff within the context of symmetric teleparallel gravity. Recently, Aditya et al. [31] examined the BT-I BHDE model in the framework of logarithmic BD gravity.

Most cosmological analyses are based on the Friedmann–Robertson–Walker (FRW) line element, which assumes perfect spatial isotropy. However, several physical processes—such as primordial anisotropies, relics of early phase transitions, or anisotropic stresses arising from dark sector physics—motivate the investigation of more general anisotropic cosmological models. Among these, the Bianchi type (BT) models represent spatially homogeneous but anisotropic cosmologies. In particular, the BT-II model is of special interest, as it is one of the simplest non-flat models that admits shear and anisotropic expansion modes while retaining analytical tractability in many scenarios. Studies of BT models are valuable for assessing the robustness of isotropization mechanisms and for identifying possible observational imprints—such as those in the cosmic microwave background (CMB) anisotropies or large-scale structure—that may provide constraints on exotic dark sector physics. The combination of anisotropic backgrounds with modified entropy or dark energy (DE) models is, therefore, well motivated, as it allows one to explore potential couplings among geometry, thermodynamics, and late-time cosmic acceleration. Alternative theories of gravity offer a complementary framework for addressing outstanding cosmological puzzles. Barber [32] introduced two continuous creation theories: one formulated as a variant of the Brans–Dicke (BD) theory, and the other as a modification of general theory of relativity (GTR) that incorporates continuous matter creation consistent with observational evidence. These models posit a universe that arises from self-contained gravitational and matter fields. Barber's second self-creation theory has inspired numerous studies of cosmological models (Refs. [33]–[37]), providing a setting in which the cosmological constant can emerge dynamically from the interaction between matter and the gravitational field. This approach offers an alternative explanation for cosmic acceleration and dark energy without invoking a constant vacuum energy density. Essentially, the theory introduces a mechanism of self-creation of gravity, which modifies both the gravitational field equations and the overall evolution of the universe. For a comprehensive treatment of dark energy and modified gravity frameworks, the reader is referred to Refs. [38]–[51]. The Self-Creation Theory (SCT), originally formulated by Barber and subsequently extended by various authors, modifies scalar–tensor gravity in such a way that matter can be created from the interplay between geometry and scalar fields, while simultaneously altering the effective gravitational coupling. SCT has been extensively investigated in the context of cosmological solutions, including Bianchi space-times, as it provides a versatile theoretical framework to study the interaction between modified gravitational dynamics and non-standard dark energy models. Combining SCT with Barrow Holographic Dark Energy (BHDE) within an anisotropic BT-*II* background allows for a unified investigation, anisotropic geometric effects, and scalar–tensor gravitational dynamics. Such an integrated approach enables the study of how these factors may influence structure formation, isotropization, and the observed late-time cosmic acceleration.

With this motivation, in this paper, we construct and analyze a spatially homogeneous BT-*II* cosmological model within the framework of SCT, where the DE sector is modelled by BHDE. We derive the modified field equations appropriate to the Self creation theory of gravity. The work is organized as follows: Section-2 contains field equations and BHDE models. Section-3 consists of observational constraints on model parameters. In section-4, we include physical discussion of our dynamical parameters. Section-5 deals with final remarks and conclusions.

2. FIELD EQUATIONS AND MODEL

We begin with the BT-II line element, which in comoving coordinates is given by

$$ds^2 = -dt^2 + \mathcal{R}(t)^2\,dx^2 + \mathcal{S}(t)^2\,dy^2 + 2\mathcal{S}(t)^2 x\,dy\,dz + \left(\mathcal{S}(t)^2x^2 + \mathcal{R}(t)^2\right)dz^2, \tag{1}$$

where $\mathcal{R}(t)$ and $\mathcal{S}(t)$ denote the directional scale factors along the x, z- and y-axes, respectively. In the framework of self-creation theory, the gravitational field equations take the form

$$R_{ij} - \tfrac{1}{2}Rg_{ij} = -\frac{8\pi}{\phi}\left(T_{ij} + \overline{T}_{ij}\right), \tag{2}$$

together with the scalar field equation

$$\Box\phi \equiv \phi^{;v}_{;v} = \frac{8\pi\mu}{3}\left(T + \overline{T}\right), \tag{3}$$

where ϕ represents the scalar field of self-creation theory, and μ is a coupling constant. The total energy-momentum distribution is split into two components: the standard matter contribution and the anisotropic DE contribution. We define the matter and DE tensors as diagonal tensors in the comoving frame (i.e., $u^i = (1,0,0,0)$, $u_i = (-1,0,0,0)$ and $u^i u_i = -1$), namely

$$T^j_i = \mathrm{diag}(-\rho_m,\,0,\,0,\,0)\,, \qquad \overline{T}^j_i = \mathrm{diag}\big(-\rho_{de},\,p_x,\,p_y,\,p_z\big)\,, \tag{4}$$

with the anisotropic EoS

$$p_x = \omega_{de}\rho_{de}, \qquad p_y = (\omega_{de} + \gamma)\rho_{de}, \qquad p_z = \omega_{de}\rho_{de}, \tag{5}$$

where ρ_m and ρ_{de} denote the energy densities of matter and DE, respectively. The parameter ω_{de} is the equation-of-state parameter of DE, while γ characterizes its anisotropic deviation along the y-direction. We stress that the skewness parameter γ introduces anisotropic diagonal pressures and does not generate shear stresses. A non-zero expression for $T^y{}_z$ would necessarily originate from a non-diagonal energy-momentum tensor (e.g. shear/tilted fluid/heat flow) which is not assumed in our formulation (since, we have a non-zero component of Einstein tensor G^y_z). In our framework, the dark-energy skewness parameter γ modifies only the diagonal pressure component p_y.

Substituting the BT-II metric (1) and the above energy-momentum components into the field equations (2)–(3) (using mixed form of these field equations), we obtain the dynamical equations governing the evolution of the anisotropic universe in self-creation theory. The mixed form is often preferred in cosmological and anisotropic models because it allows a direct physical interpretation of the energy density and directional pressures. These equations explicitly couple the scale factors $\mathcal{R}(t)$, $\mathcal{S}(t)$, and the scalar field $\phi(t)$, thereby allowing us to study the impact of anisotropic DE on the cosmological dynamics.

$$\frac{\ddot{\mathcal{S}}}{\mathcal{S}} + \frac{\dot{\mathcal{R}}}{\mathcal{R}}\frac{\dot{\mathcal{S}}}{\mathcal{S}} + \frac{\ddot{\mathcal{R}}}{\mathcal{R}} + \frac{\mathcal{S}^2}{4\mathcal{R}^4} = \frac{-8\pi\omega_{de}\rho_{de}}{\phi} \tag{6}$$

$$\frac{2\ddot{\mathcal{R}}}{\mathcal{R}} + \frac{\dot{\mathcal{R}}^2}{\mathcal{R}^2} - \frac{3\mathcal{S}^2}{4\mathcal{R}^4} = \frac{-8\pi(\omega_{de}+\gamma)\rho_{de}}{\phi} \tag{7}$$

$$\frac{2\dot{\mathcal{R}}\dot{\mathcal{S}}}{\mathcal{R}\mathcal{S}} + \frac{\dot{\mathcal{R}}^2}{\mathcal{R}^2} - \frac{\mathcal{S}^2}{4\mathcal{R}^4} = \frac{8\pi[\rho_m+\rho_{de}]}{\phi} \tag{8}$$

$$\dot{\phi}\left(\frac{2\dot{\mathcal{R}}}{\mathcal{R}} + \frac{\dot{\mathcal{S}}}{\mathcal{S}}\right) + \ddot{\phi} = \frac{8\pi\mu(T+\overline{T})}{3}. \tag{9}$$

Differentiation with respect to time t is represented by a dot above a variable in this notation. The non-diagonal Einstein tensor satisfies the geometric identity

$$G^y{}_z = -x\left(-\frac{\ddot{\mathcal{S}}}{\mathcal{S}} + \frac{\ddot{\mathcal{R}}}{\mathcal{R}} + \frac{\dot{\mathcal{R}}^2}{\mathcal{R}^2} - \frac{\mathcal{S}^2}{\mathcal{R}^4} - \frac{\dot{\mathcal{R}}\dot{\mathcal{S}}}{\mathcal{R}\mathcal{S}}\right) = x\left(G^y_y - G^x_x\right), \tag{10}$$

which follows from the specific non-diagonal structure of the metric. Hence, the mixed Einstein equation is not independent and can be obtained from the difference of the diagonal field equations. The total energy–momentum tensor employed in Eq. (4) which represents an anisotropic dark energy component together with pressureless matter. Using field equations (expressed in mixed form by raising the indices in Eq. (2)),

$$G^j{}_i = -\frac{8\pi}{\phi}T^j{}_i, \tag{11}$$

the difference of the yy and xx components yields

$$G^y{}_y - G^x{}_x = -\frac{8\pi}{\phi}\left(T^y{}_y - T^x{}_x\right) = -\frac{8\pi}{\phi}\,\gamma\,\rho_{de}. \tag{12}$$

Therefore, the off-diagonal field equation $G^y{}_z = -\frac{8\pi}{\phi}T^y{}_z$ is automatically satisfied and does not introduce an additional independent constraint. We can solve the system of equations (6)-(8) appropriately with the use of assumptions which connects unknowns in the field equations. Because of this, we take into account the following physically plausible circumstances:

$$\mathcal{R} = \mathcal{S}^k. \tag{13}$$

In this framework, k represents a constant (Collins et al. [52]). Observational studies of velocity–redshift relations from extragalactic sources reveal that the present cosmic expansion is isotropic to within nearly 30% [53, 54, 55]. Complementary redshift surveys further constrain the shear-to-expansion ratio, yielding $\frac{\sigma}{H} \leq 0.3$ within our Galaxy at the current epoch. A widely employed approach in scalar–tensor cosmologies is to relate the scalar field ϕ to the average scale factor $a(t)$ through a simple power-law ansatz [56, 57]:

$$\phi \propto a(t)^n,$$

where n is a dimensionless index. This relation has been extensively investigated in the literature, as it captures a range of possible scalar-field behaviors with remarkable simplicity [58]-[63]. Motivated by both its mathematical tractability and its physical plausibility, we adopt the following specific assumption in our analysis:

$$\phi(t) = \phi_0[a(t)]^n. \tag{14}$$

Using the relations (13) and (14) in Eqs. (6) and (7), we obtain the metric potentials as

$$\mathcal{R} = (b_3 e^{\gamma_0 t} + b_4)^{\frac{1}{k+2}} \tag{15}$$

and

$$\mathcal{S} = (b_3 e^{\gamma_0 t} + b_4)^{\frac{k}{k+2}} \tag{16}$$

where $b_3 = \frac{(k+2)b_1}{\gamma_0}$, $b_4 = (k+2)b_2$, b_1 and b_2 are integrating constants. The scalar field of the model is

$$\phi = \phi_0 \left(b_3 e^{\gamma_0 t} + b_4\right)^{\frac{n}{3}}. \tag{17}$$

Now metric (1), with the aid of Eqs. (15) and (16), can be written as

$$\begin{aligned} ds^2 = -dt^2 + (b_3 e^{\gamma_0 t} + b_4)^{\frac{2}{k+2}} dx^2 + (b_3 e^{\gamma_0 t} + b_4)^{\frac{2k}{k+2}} dy^2 + 2(b_3 e^{\gamma_0 t} + b_4)^{\frac{2k}{k+2}} x dy dz \\ +((b_3 e^{\gamma_0 t} + b_4)^{\frac{2k}{k+2}} x^2 + (b_3 e^{\gamma_0 t} + b_4)^{\frac{2}{k+2}}) dz^2. \end{aligned} \tag{18}$$

Equation (18) describes a anisotropic BT-II BHDE model within the context of self-creation gravity theory, with the following physical parameters. The model's average scale factor $a(t)$ and volume $V(t)$ are defined as follows:

$$V(t) = a(t)^3 = (b_3 e^{\gamma_0 t} + b_4). \tag{19}$$

The expressions for the mean Hubble H and the expansion scalar θ parameters are derived as follows:

$$\begin{aligned} H = 3\theta &= \frac{b_3 \gamma_0 e^{\gamma_0 t}}{3\, b_3 e^{\gamma_0 t} + 3\, b_4} \\ &= \frac{\gamma_0}{3}\left[1 - b_4(1+z)^3\right] = \frac{H_0}{1-b_4}\left[1 - b_4(1+z)^3\right]. \end{aligned} \tag{20}$$

where $1 + z = \frac{1}{a(t)}$ and $a(t)$ is average scale factor. Here $\frac{H_0}{1-b_4} = \frac{\gamma_0}{3}$. We will constrain following parameters H_0 and b_4 with observational datasets in section-3. We will evaluate the parameters γ_0 and k from the expression $\gamma_0 = \frac{3H_0}{1-b_4}$, and $k = \frac{b_4}{b_2} - 2$ for appropriate choice of arbitrary integrating constant b_2 and observationally constrained values of H_0 and b_4. The average anisotropic parameter A_h and shear scalar σ^2 are given by

$$\sigma^2 = \frac{(k-1)^2 b_3^2 \gamma_0^2 e^{2\gamma_0 t}}{(k+2)^2 (b_3 e^{\gamma_0 t} + b_4)^2}\ ;\ \ A_h = \frac{2(k-1)^2}{(k+2)^2}. \tag{21}$$

From the obtained solutions, it is clear that the spatial volume of the universe undergoes an exponential increase, which reflects the accelerated expansion characteristic of the present cosmic epoch. During the initial stages of cosmic evolution, all dynamical quantities such as the scale factors, expansion scalar, and energy densities remain finite, thereby avoiding any initial singularity. As cosmic time progresses, i.e., in the limit $t \to \infty$, these quantities diverge, indicating the unbounded growth of the universe in accordance with an accelerated expansion scenario. A particularly interesting case emerges when $k = 1$. In this situation, the model becomes shear-free and isotropic, as demonstrated by the vanishing conditions $\sigma^2 = 0$ and $A_h = 0$. This implies that the anisotropic contributions completely disappear, and the model smoothly reduces to the isotropic case, which is consistent with the standard FLRW cosmology. Such a limiting behavior is significant, since it shows that the present anisotropic model can naturally accommodate isotropy under specific parameter choices, in agreement with observational evidence from CMB measurements and large-scale structure surveys that strongly favor an isotropic universe on large scales.

BHDE: The conventional formulation of HDE employs the Hubble horizon as the IR cutoff and makes use of the Bekenstein–Hawking area law to determine the horizon of the Universe. However, this framework falls short in reproducing the full cosmic evolution, which has motivated several modifications. These adjustments typically involve either adopting alternative IR cutoffs or modifying the entropy–area relation. In this context, an HDE model inspired by Barrow entropy has attracted considerable attention in recent years. Barrow proposed that quantum gravity effects may alter the

geometry of black hole horizons, imparting them with intricate, fractal-like features. Such corrections render the entropy formula more general, leading to the expression

$$S \sim \mathcal{A}^{1+\delta/2}, \tag{22}$$

where $0 \leq \delta \leq 1$. The cases $\delta = 0$ and $\delta = 1$ correspond to the standard entropy–area law and the maximal deviation from it, respectively. Notably, observational bounds on δ have already been obtained. Building on Eq. (22) and the profound link between gravity and thermodynamics, Barrow's framework has been extended to cosmology. In particular, the DE density in the Barrow HDE scenario is given by

$$\rho_{de} = C\,\mathcal{L}^{\delta-2}, \tag{23}$$

where the constant $C = 3c^2M_p^2$ has dimensions $[\mathcal{L}]^{2-\delta}$. Here, c is a numerical parameter and $M_p^2 = \frac{1}{8\pi G}$ denotes the reduced Planck mass. Within the framework of self creation theory of gravity, since $\frac{1}{G} = \phi$, one obtains $C = \frac{3c^2\phi}{8\pi}$.

Model-1: BHDE model with Hubble horizon

The IR cutoff determines the largest scale that contributes to the energy density in HDE. In the standard HDE framework, the choice of IR cutoff (such as the event horizon, particle horizon, or Hubble horizon) significantly influences the cosmic dynamics. Unlike the event horizon, which depends on the future evolution of the scale factor, the Hubble horizon is locally defined. This feature allows it to avoid the causality problem, thereby making it a more physically consistent choice in certain cosmological scenarios. In the BHDE model, adopting the Hubble radius as the IR cutoff provides a local, causal, and observationally viable description of DE. By setting the IR cutoff as $\mathcal{L} = \frac{1}{H}$, we obtain

$$\rho_{de} = CH^{2-\delta} \tag{24}$$

where Hubble parameter H is given by Eq. (20). Using Hubble parameter (20) in Eq. (24), we obtain the energy density of BHDE with Hubble horizon as IR cutoff as

$$\rho_{de} = \frac{3c^2\phi_0\,(b_3e^{\gamma_0 t}+b_4)^{\frac{n}{3}}}{8\pi}\left[\frac{\gamma_0}{3}\left[1-b_4(1+z)^3\right]\right]^{2-\delta}. \tag{25}$$

The BT-II universe with BHDE with Hubble horizon inside the framework of self-creation theory of gravity is shown by Eq. (18), the scalar field (17), and the energy density (25). Using Eqs. (6), (15)-(17) and (25), we get EoS parameter as

$$\begin{aligned}\omega_{de} = -\frac{1}{3c^2}\Bigg(&\frac{b_3^2\gamma_0^2\,e^{2\gamma_0 t}}{(k+2)^2\,(b_3e^{\gamma_0 t}+b_4)^2}+\frac{b_3b_4\gamma_0^2\,e^{\gamma_0 t}}{(k+2)\,(b_3e^{\gamma_0 t}+b_4)^2}+\frac{k^2b_3^2\gamma_0^2\,e^{2\gamma_0 t}}{(k+2)^2\,(b_3e^{\gamma_0 t}+b_4)^2}+\frac{k\,b_3b_4\gamma_0^2\,e^{\gamma_0 t}}{(k+2)\,(b_3e^{\gamma_0 t}+b_4)^2}\\&+\frac{k\,b_3^2\gamma_0^2\,e^{2\gamma_0 t}}{(k+2)^2\,(b_3e^{\gamma_0 t}+b_4)^2}+\frac{1}{4}\,\frac{\left((b_3e^{\gamma_0 t}+b_4)^{\frac{k}{k+2}}\right)^2}{\left((b_3e^{\gamma_0 t}+b_4)^{(k+2)^{-1}}\right)^4}\Bigg)\times\left(\left(\frac{b_3\gamma_0e^{\gamma_0 t}}{3\,(b_3e^{\gamma_0 t}+b_4)}\right)^{2-\delta}\right)^{-1}.\end{aligned} \tag{26}$$

and we find the skewness parameter as

$$\gamma = \frac{1}{3c^2}\left(\left((b_3e^{\gamma_0 t}+b_4)^{\frac{1}{k+2}}\right)^{2k-4}+\frac{(k-1)\,\gamma_0^2\,b_3e^{\gamma_0 t}}{(k+2)\,(b_3e^{\gamma_0 t}+b_4)}\right)\left(\left(\frac{b_3\gamma_0e^{\gamma_0 t}}{3(b_3e^{\gamma_0 t}+b_4)}\right)^{2-\delta}\right)^{-1}. \tag{27}$$

Model-2: BHDE model with Granda–Oliveros horizon

The Granda–Oliveros (GO) cutoff is determined by the present value of the Hubble parameter H and its time derivative $\dot{H}$. Unlike the event horizon cutoff, it avoids issues of non-locality and causality, since the presence of $\dot{H}$ introduces a dynamical component that allows the DE density to evolve naturally. Moreover, because it does not involve integration over the future cosmic time, the GO cutoff is regarded as physically more realistic and more consistent with both thermodynamics and causality. In this framework, we consider the BHDE model with the GO horizon cutoff defined as $\mathcal{L} = \left(\alpha_1H^2+\alpha_2\dot{H}\right)^{-\frac{1}{2}}$, (Granda and Oliveros [64, 65]), and hence we obtain

$$\rho_{de} = \frac{3}{8}\,\frac{c^2\phi_0\left(b_3e^{\gamma_0 t}+b_4\right)^{\frac{n}{3}}}{\pi}\left(\frac{\alpha_1\,b_3^2\gamma_0^2\,e^{2\gamma_0 t}}{\left(3b_3e^{\gamma_0 t}+3b_4\right)^2}+\frac{1}{3}\,\frac{\alpha_2\,b_3b_4\gamma_0^2\,e^{\gamma_0 t}}{\left(b_3e^{\gamma_0 t}+b_4\right)^2}\right)^{1-\frac{\delta}{2}} \tag{28}$$

The BT-II universe with BHDE with GO horizon inside the framework of self-creation theory of gravity is shown by Eq. (18), the scalar field (17), and the energy density (28). Using Eqs. (6), (15)-(17) and (28), we get EoS parameter as

$$\omega_{de} = -\frac{1}{3c^2}\left[\frac{b_3^2\gamma_0^2e^{2\gamma_0 t}}{(k+2)^2(b_3e^{\gamma_0 t}+b_4)^2}+\frac{(k+1)b_3b_4\gamma_0^2e^{\gamma_0 t}}{(k+2)(b_3e^{\gamma_0 t}+b_4)^2}+\frac{(k^2+k)b_3^2\gamma_0^2e^{2\gamma_0 t}}{(k+2)^2(b_3e^{\gamma_0 t}+b_4)^2}\right.$$

$$+\frac{1}{4}\frac{\left((b_3e^{\gamma_0 t}+b_4)^{\frac{k}{k+2}}\right)^2}{\left((b_3e^{\gamma_0 t}+b_4)^{\frac{1}{k+2}}\right)^4}\Bigg]\times\left(\frac{\alpha_1 b_3^2\gamma_0^2e^{2\gamma_0 t}}{(3b_3e^{\gamma_0 t}+3b_4)^2}+\frac{1}{3}\frac{\alpha_2 b_3 b_4\gamma_0^2e^{\gamma_0 t}}{(b_3e^{\gamma_0 t}+b_4)^2}\right)^{\frac{\delta}{2}-1} \tag{29}$$

we find the skewness parameter as

$$\gamma=\frac{1}{3c^2}\left[\left((b_3e^{\gamma_0 t}+b_4)^{\frac{1}{k+2}}\right)^{2k-4}+\frac{(k-1)\gamma_0^2b_3e^{\gamma_0 t}}{(k+2)(b_3e^{\gamma_0 t}+b_4)}\right]\left(\frac{\alpha_1 b_3^2\gamma_0^2e^{2\gamma_0 t}}{(3b_3e^{\gamma_0 t}+3b_4)^2}+\frac{1}{3}\frac{\alpha_2 b_3 b_4\gamma_0^2e^{\gamma_0 t}}{(b_3e^{\gamma_0 t}+b_4)^2}\right)^{\frac{\delta}{2}-1}. \tag{30}$$

3. OBSERVATIONAL CONSTRAINTS

The field equations with anisotropic DE in the framework of self-creation theory of gravity have been solved in closed form, leading to a cosmological model in which the Hubble parameter depends explicitly on the parameters (H_0, b_4). To test the viability of this solution in describing the present Universe, we employ observational Hubble datasets to constrain the model parameters. For this purpose, we use a joint compilation of 31 Hubble parameter measurements obtained from cosmic chronometer (CC) observations [66, 67]. To explore the parameter space around the local minima, we carry out a numerical analysis with the `emcee` package in Python, adopting Gaussian priors centered on the initial estimates with a fixed standard deviation of $\sigma = 1.0$. The statistical analysis is based on the chi-square estimator, defined as

$$\chi^2_H(H_0,b_4)=\sum_{i=1}^{31}\frac{[H_{\rm th}(z_i;H_0,b_4)-H_{\rm obs}(z_i)]^2}{\sigma^2_{H(z_i)}}, \tag{31}$$

where $H_{\rm obs}(z_i)$ denotes the observed Hubble parameter at redshift z_i, $H_{\rm th}(z_i;H_0,b_4)$ is the theoretical prediction of the model, and $\sigma_{H(z_i)}$ represents the corresponding observational uncertainty. Using this dataset, we obtain the best-fit values of the parameters H_0 and b_4. The constraints are derived through a Markov Chain Monte Carlo (MCMC) analysis, ensuring a robust estimation of the model parameters in light of current observational data.

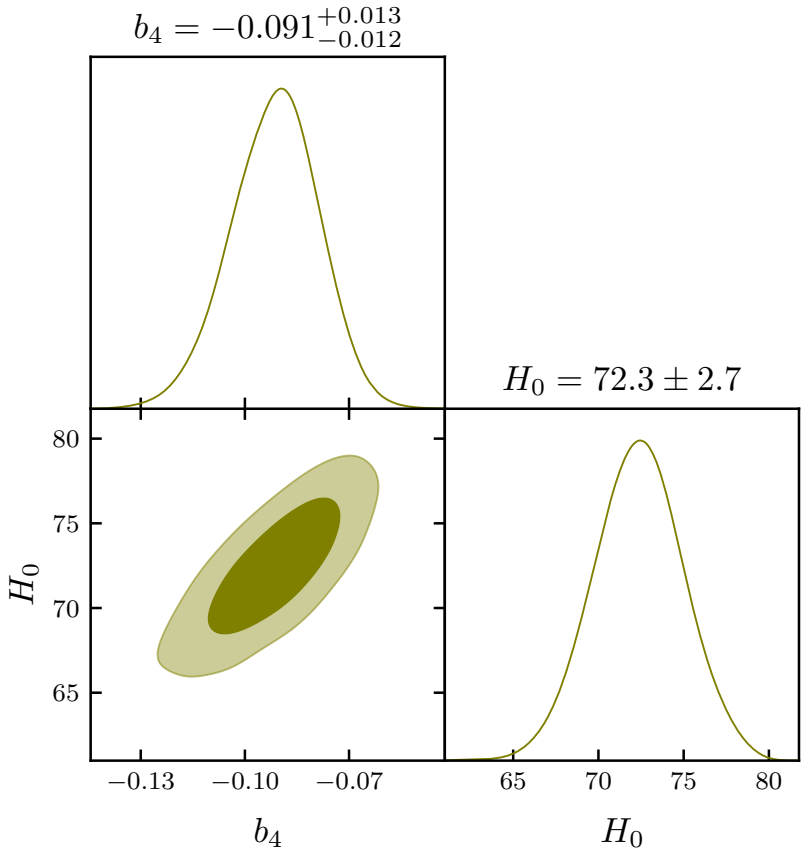

Figure 1. The plot displays the 2D contour plots of the model parameters.

In order to test the validity of the proposed BHDE models, we have constrained the free parameters using Hubble cosmic chronometer (CC) data. The joint analysis provides best-fit values for the model parameter and the present Hubble

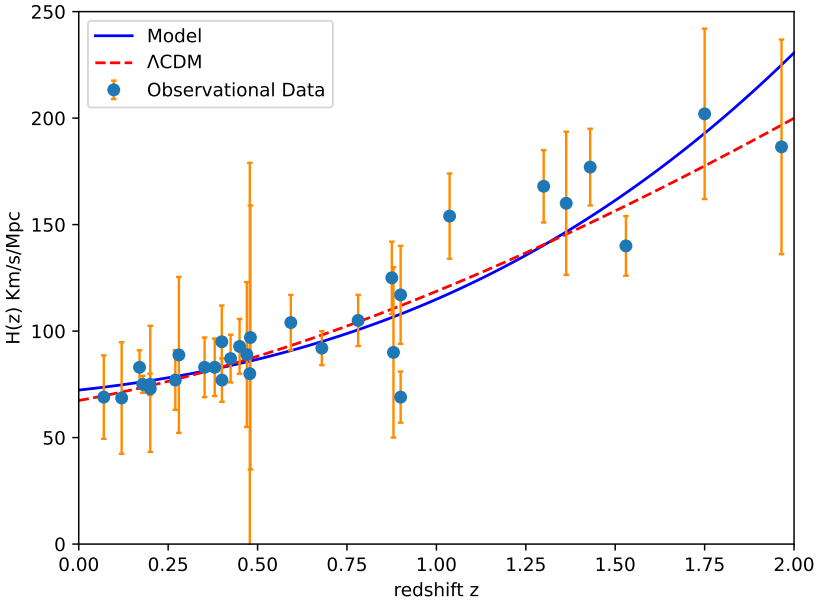

Figure 2. Evolution of Hubble parameter $H(z)$ versus redshift z. The solid line represents our model and dotted-line indicates the ΛCDM model with $\Omega_{m0} = 0.3$ and $\Omega_{\Lambda 0} = 0.7$. The dots are shown the Hubble dataset with error bar.

constant as

$$b_4 = -0.091^{+0.013}_{-0.012}, \qquad H_0 = 72.3 \pm 2.7 \text{ km s}^{-1}\text{Mpc}^{-1}.$$

Fig. 1 displays the contour plots in the b_4–H_0 parameter space. The contours show a well-defined and narrow confidence region, implying that both b_4 and H_0 are tightly constrained by the CC dataset. Fig. 2 illustrates the theoretical prediction of the Hubble parameter $H(z)$ for the best-fit model, along with the observational Hubble data points and the standard ΛCDM curve for comparison. The model curve exhibits excellent agreement with the observational Hubble data across the redshift range $0 < z < 2$, confirming its consistency with the observed expansion history. The combination of low-z ΛCDM-like behaviour and high-z deviations highlights the dynamical nature of BHDE, which interpolates between standard expansion and phantom-like regimes.

4. COSMOLOGICAL PARAMETERS

In this section, we analyze the expansion behavior of the universe for the constructed BHDE models (Model-1 and Model-2) using well-established cosmological diagnostics, including the EoS parameter ω_{de}, the squared sound speed v_s^2, the deceleration parameter q. Additionally, we employ cosmological diagnostic planes such as $\omega_{de} - \omega'_{de}$, the statefinder pair (r, s), and the $r - q$ plane. Here, we have used the parameter values as $\gamma_0 = 0.62$, $n = -0.964$, $b_1 = 0.3$, $b_2 = -0.03063$, $b_4 = -0.091^{+0.013}_{-0.012}$, $H_0 = 72.3 \pm 2.7$, $\lambda = 10.02$, $\phi_0 = 40.021$, $w = 60.1$, $k = 0.98$, $c = 0.65$, $\delta = 0.66$, $\alpha_1 = 0.98$, $\alpha_2 = 0.01$ for graphical representation of the dynamical parameters of the models.

Scalar field: Fig. 3 shows the evolution of the scalar field $\phi(z)$ as a function of redshift z, where the shaded region represents the 1σ confidence interval obtained for the parameter $b_4 = -0.091^{+0.013}_{-0.012}$. The scalar field increases monotonically with redshift, starting from small values at $z < 0$ (future epoch) and attaining progressively larger values at higher redshifts ($z > 1$). This trend indicates that the scalar field was dynamically significant in the early Universe and gradually decreased in relative strength toward the present epoch. The shaded area in the plot quantifies the effect of uncertainties in b_4. Near the present epoch ($z \approx 0$), the uncertainty is minimal, indicating that the scalar field behaviour is well constrained by observations. At higher redshifts ($z > 2$), the spread grows wider, reflecting the cumulative impact of parameter uncertainties on the early-time evolution of $\phi(z)$. The increasing scalar field amplitude in the past suggests its dominance during the anisotropic early Universe, possibly contributing to structure formation or stiff-fluid–like dynamics. Toward late times, the reduction in $\phi(z)$ signifies its transition to a subdominant role. The constrained negative value of b_4 ensures consistency with this transition while still allowing for a dynamical scalar field contribution.

Deceleration parameter: The deceleration parameter

$$q(z) = -\frac{\ddot{a}\,a}{\dot{a}^2} = -1 - \frac{3b_4}{b_3 e^{\gamma_0 t}} \tag{32}$$

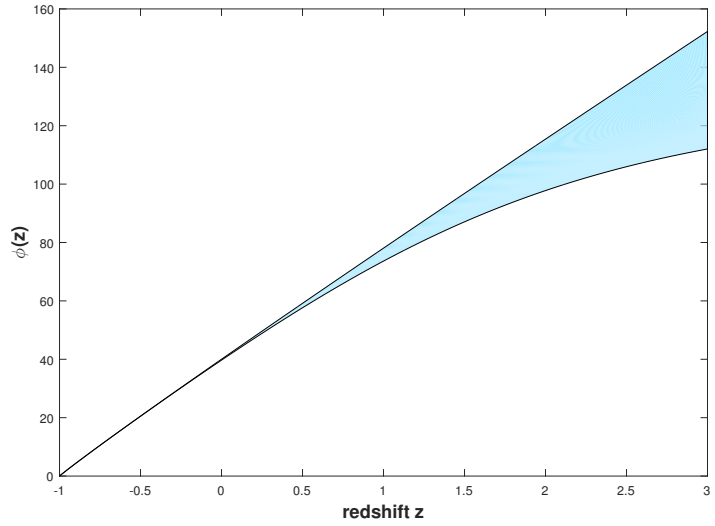

Figure 3. Plot of scalar field versus redshift.

encodes the kinematic state of cosmic expansion: $q > 0$ denotes a decelerating universe, $q = 0$ a uniform expansion rate, and $q < 0$ an accelerating expansion.

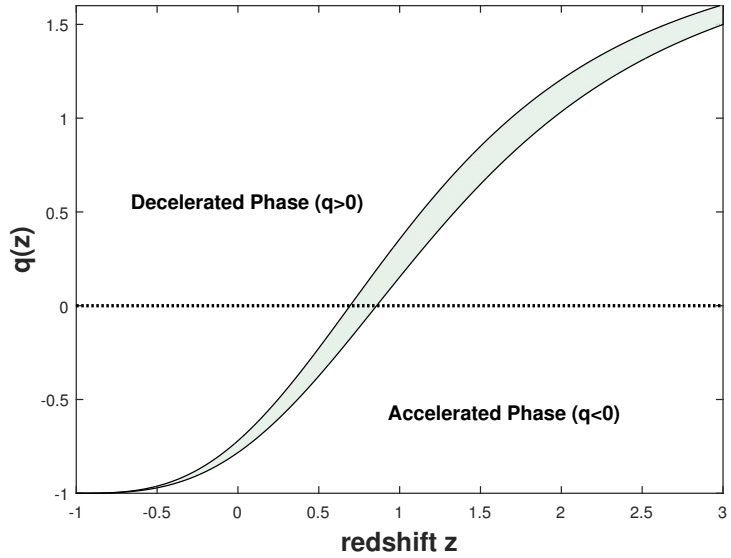

Figure 4. Deceleration parameter versus redshift.

The plotted curve of $q(z)$ with the shaded band in Fig. 4 shows both the best–fit evolution and the 1σ uncertainty corresponding to the fitted parameter $b_4 = -0.091^{+0.013}_{-0.012}$. The small uncertainty on b_4 indicates that the data set used for the fit tightly constrains the model direction controlled by this parameter. The narrow shaded region around the central curve implies that the inferred shape of $q(z)$ is robust against modest changes in model parameters. The curve clearly shows $q(z) > 0$ at sufficiently large redshift, signaling the expected decelerated expansion in the matter (and earlier radiation) dominated epochs. At lower redshifts the curve crosses $q = 0$ and becomes negative, indicating a transition to accelerated expansion. The transition (or transition redshift z_t) lies in the intermediate redshift range (roughly of order unity), marking the epoch when the dark–energy–like component began to dominate the expansion dynamics. At the present epoch ($z \approx 0$) the curve lies in the $q < 0$ region, consistent with a presently accelerating Universe. The shaded band shows that the sign and magnitude of q_0 are determined with good precision. It can be seen that our models decelerates at high z, a transition at $z \sim 1$, and acceleration at low z which is in agreement with independent probes such as SNe Ia, BAO and CC measurements.

Statefinder parameters: Various DE models have emerged in recent years, aiming to elucidate the accelerating ex-

pansion of the universe. Interestingly, these models often yield identical values for the current Hubble and deceleration parameters, making them practically indistinguishable from one another. Sahni et al. [68] proposed a merger of the deceleration and Hubble parameters, expressed as:

$$r=\frac{\dddot{a}}{aH^3}, \quad s=\frac{r-1}{3(q-1/2)}. \tag{33}$$

The statefinder parameters for our model are

$$r = 1+\frac{9{b_4}^2}{{b_3}^2\left(e^{\gamma_0 t}\right)^2} \tag{34}$$

$$s = \frac{{b_4}^2}{{b_3}^2\left(e^{\gamma_0 t}\right)^2}\left(-\frac{1}{2}-\frac{b_4}{b_3 e^{\gamma_0 t}}\right)^{-1} \tag{35}$$

Fig. 5 displays the trajectories of the models in the (r, s) diagnostic plane, which provide powerful geometrical tools to distinguish different DE scenarios from one another and from the concordance ΛCDM model. The statefinder pair (r, s) is defined in terms of higher derivatives of the scale factor and is particularly effective in discriminating among DE models. The ΛCDM model corresponds to the fixed point $(r, s) = (1, 0)$, while the CDM model lies at $(r, s) = (1, 1)$. The trajectories in the figure show that the model under consideration evolves away from the ΛCDM fixed point, moving through different evolutionary regimes. The sign of s carries important physical meaning. For $s > 0$, the trajectory indicates a phantom-like behaviour of DE, whereas $r < 1$ corresponds to the quintessence regime. The region $s < 0$ with $r > 1$ is characteristic of the Chaplygin gas model, representing a unified description of dark matter and DE. The trajectory's excursion into this domain indicates that the model mimics Chaplygin-like behaviour during certain epochs.

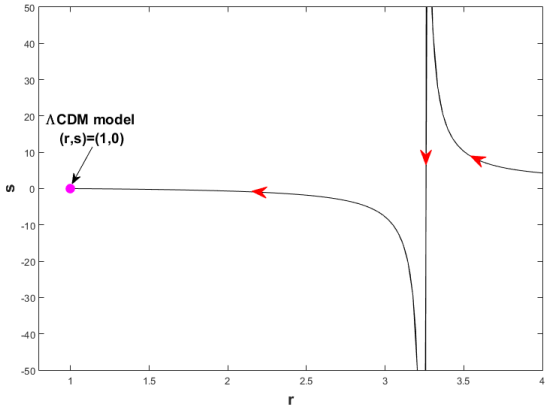

Figure 5. Plot of $r - s$ plane.

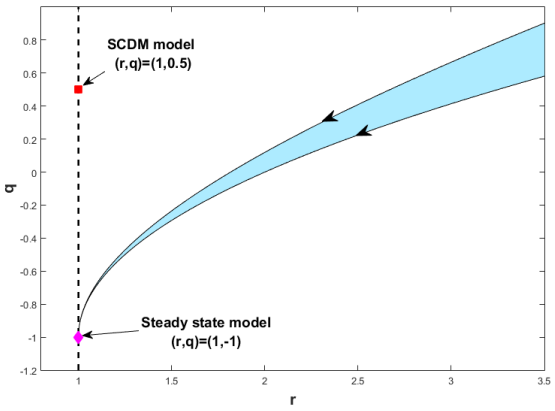

Figure 6. Plot of $r - q$ plane.

(r, q) **plane:** The (r, q) diagnostic provides another valuable tool for testing the dynamical behaviour of cosmological models, particularly in distinguishing between decelerating and accelerating phases. Fig. 6 gives the behavior of our model in $r - q$ plane. Two fixed points are of particular interest: $(r, q) = (1, 0.5)$, corresponding to the standard cold dark matter (SCDM) model without a cosmological constant, and $(r, q) = (1, -1)$, corresponding to the de Sitter model. The trajectories in the (r, q) plane clearly illustrate the transition from the decelerating matter-dominated epoch to the accelerating DE-dominated epoch. The shaded region corresponds to the uncertainty arising from the fitted model parameters and highlights the robustness of this transition. The arrows on the curves indicate the evolutionary direction, showing that the Universe starts near the SCDM point at high redshift and evolves towards the de Sitter attractor at late times.

Skewness parameter: Figs. 7 and 8 illustrate the behaviour of the skewness (or deviation) parameter γ as a function of redshift for both model-1 and model-2. The parameter γ quantifies the deviation of the DE EoS from its isotropic counterpart and therefore serves as a diagnostic tool for identifying anisotropies, departures from ΛCDM, and higher-order dynamical corrections. In both models, γ increases with redshift, reaches a peak around $z \sim 1$–2, and then saturates or decreases at higher redshift. This peak corresponds to the transition epoch from deceleration to acceleration, indicating that anisotropic effects and deviations from the canonical EoS are most pronounced during this phase. In the late Universe, $\gamma \to 0$, implying that the DE component behaves isotropically and resembles the standard ΛCDM model. This result is consistent with present observational constraints that strongly favour isotropy and $\omega_{de} \approx -1$ in the current epoch. At early times, the value of γ decreases again, reflecting the dominance of the matter component over DE. This indicates

that anisotropic deviations become less significant when the Universe approaches the standard matter-dominated evolution. Both models exhibit similar qualitative trends, but subtle differences are evident. Model-1 produces slightly larger uncertainty bands and stronger anisotropic deviations at higher z, whereas model-2 yields a narrower confidence region and smoother evolution of γ. This suggests that the model-2 provides a more stable description of anisotropic departures from ΛCDM and is therefore better aligned with current observational data.

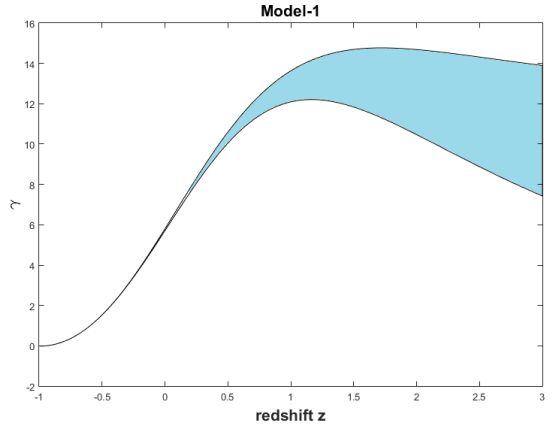

Figure 7. Plot of skewness parameter versus redshift for model-1.

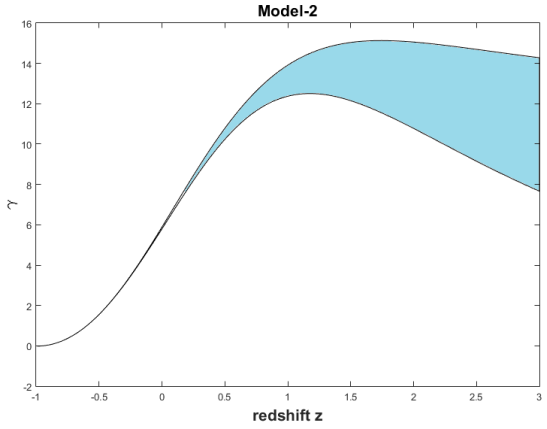

Figure 8. Plot of skewness parameter versus redshift for model-2.

Energy conditions: The Raychaudhuri equations initiated the exploration of energy conditions, playing a crucial role in analyzing the alignment of null and time-like geodesics. The energy conditions are used to illustrate other universal principles about the dynamics of intense gravitational fields. The often observed energy conditions are as follows:

Dominant energy condition (DEC): $\rho_{de} \geq 0$, $\rho_{de} \pm p_{de} \geq 0$.
Strong energy conditions (SEC) : $\rho_{de} + p_{de} \geq 0$, $\rho_{de} + 3p_{de} \geq 0$,
Null energy conditions (NEC): $\rho_{de} + p_{de} \geq 0$,
Weak energy conditions (WEC): $\rho_{de} \geq 0$, $\rho_{de} + p_{de} \geq 0$,

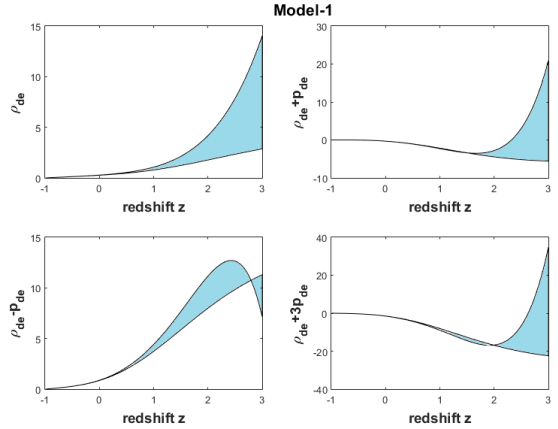

Figure 9. Plot of energy conditions versus redshift for model-1.

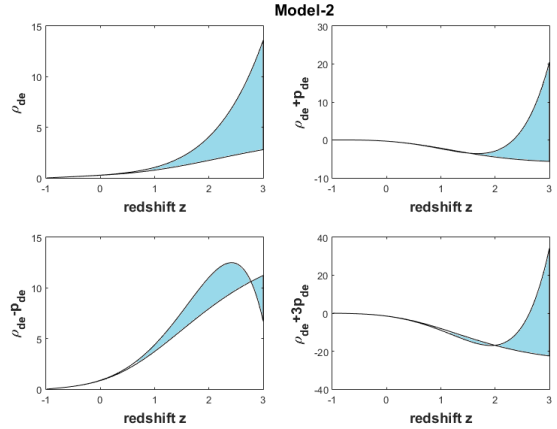

Figure 10. Plot of energy conditions versus redshift for model-2.

Figs. 9 and 10 show the behaviour of various combinations of the DE density and pressure that are directly related to the classical energy conditions. The shaded regions correspond to the 1σ confidence interval due to the constraint $b_4 = -0.091^{+0.013}_{-0.012}$. The following points are the implications for the dominant, strong, null, and weak energy conditions in both model-1 and model-2. The WEC requires $\rho_{de} \geq 0$ and $\rho_{de} + p_{de} \geq 0$. From the plots, ρ_{de} remains strictly positive throughout the redshift range for both models, ensuring that the first part of the WEC is always satisfied. However, the condition $\rho_{de} + p_{de} \geq 0$ shows periods of violation at intermediate and high redshifts, particularly in model-1, reflecting the phantom-like behaviour of DE in those epochs. The NEC has the same requirement as the second part of the WEC, i.e. $\rho_{de} + p_{de} \geq 0$. In both models, NEC is violated when the evolution of ω_{de} dips into the phantom regime ($\omega_{de} < -1$). The DEC requires $\rho_{de} \geq 0$ and $\rho_{de} \pm p_{de} \geq 0$. As noted, $\rho_{de} \geq 0$ is always satisfied. However, $\rho_{de} - p_{de}$ (not explicitly

plotted) is easily satisfied since p_{de} is negative in most of the evolution. The critical test is $\rho_{de} + p_{de} \geq 0$, which, as discussed, is violated in the phantom era. Therefore, DEC is violated in epochs where the models enter deep phantom behaviour, more prominently in model-1. The SEC requires $\rho_{de} + p_{de} \geq 0$ and $\rho_{de} + 3p_{de} \geq 0$. The plots clearly show that $\rho_{de} + 3p_{de}$ becomes negative at low redshift in both models, indicating a violation of SEC in the late-time Universe. This violation is essential to drive accelerated expansion, consistent with the requirement for a negative effective pressure. In the high-redshift regime, the SEC can be partially restored, though the uncertainty bands suggest that the violation remains robust across most of the evolution. Both models share the same qualitative features with respect to the energy conditions, but the strength of violation differs. Model-1 shows stronger and more prolonged violations of NEC, WEC, and SEC, consistent with its deeper phantom excursions. Model-2, by contrast, exhibits milder violations and tends to stay closer to the boundary of the conditions.

EoS parameter (ω_{de}): It serves as a crucial tool for categorizing the various phases in the expanding universe. It is expressed as $\omega = \frac{p}{\rho}$, representing the relationship between pressure (p) and energy density (ρ) within a given matter distribution. Different phases, characterized by deceleration or acceleration, correspond to specific ranges of ω. Deceleration phases encompass intervals such as those involving cold dark matter or dust fluid (ω equals zero), indicating the radiation era when ω lies between 0 and $1/3$, and the fluid is classified as stiff for $\omega = 1$. The accelerating phase, akin to the cosmic constant/vacuum period (ω equals -1), corresponds to the quintessence period when $-1 < \omega < -1/3$, and it's known as the phantom era when $\omega < -1$. This signifies a quintom period characterized by a combination of both quintessence and phantom components.

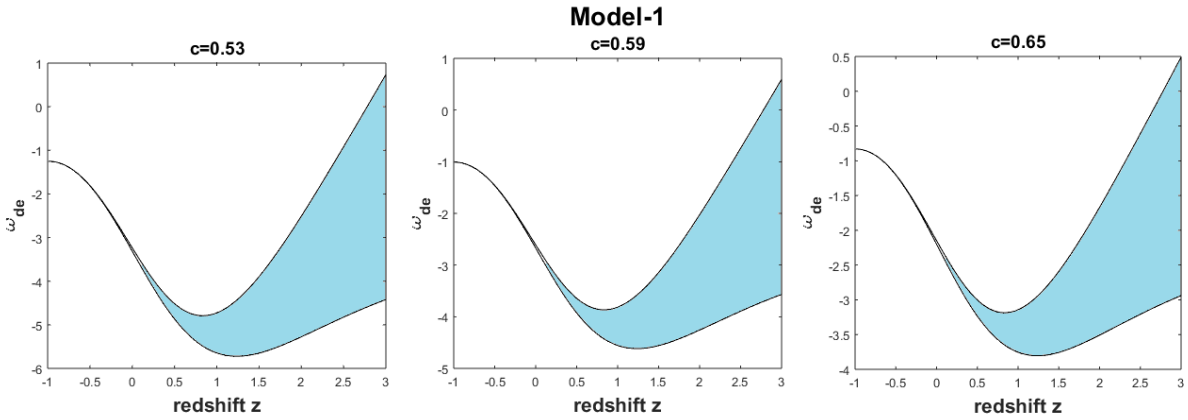

Figure 11. Plot of EoS parameter versus redshift for model-1.

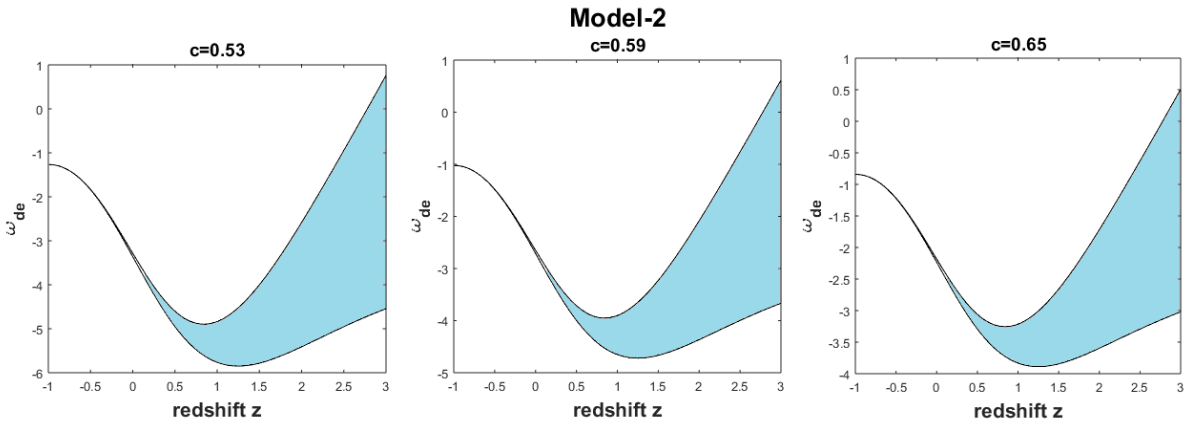

Figure 12. Plot of EoS parameter versus redshift for model-2.

Figs. 11 and 12 display the redshift evolution of the BHDE EoS parameter $\omega_{de}(z)$ for two models-1 & 2. Each panel shows the best–fit curve (solid line) and the 1σ uncertainty band for three representative values of the BHDE parameter c (here $c = 0.53, 0.59, 0.65$). Both models exhibit a strongly dynamical $\omega_{de}(z)$: the EoS begins near $\omega_{de} \simeq -1$ at very low redshift, steepens into a pronounced phantom regime ($\omega_{de} < -1$) at intermediate redshifts, reaches a minimum value typically around $z \sim 1$, and then turns upward at higher redshift. This nontrivial evolution indicates that the BHDE scenarios considered are dynamical DE models rather than simple cosmological constant models. Although the two model

types share the same qualitative trend, model-2 generally produces milder phantom regime than model-1 for the same values of c. Increasing c (from 0.53 to 0.65 in the panels) systematically shifts $\omega_{de}(z)$ upward, i.e. towards less phantom (closer to -1) behaviour. For each model the smallest c gives the deepest phantom dip, whereas larger c softens the deviation. This monotonic dependence highlights that the BHDE parameter controls the strength of dynamical effects: larger c weakens the departure from a cosmological constant. At low redshift the models are close to the cosmological constant ($\omega \approx -1$); at intermediate redshift they enter the phantom domain ($\omega < -1$); and at sufficiently high redshift they approach less negative values. Because ω_{de} can cross the phantom divide ($\omega = -1$) during evolution, the model naturally realizes a quintom-like behaviour (i.e., a combination of quintessence and phantom characteristics over cosmic history).

$\omega_{de}-\omega'_{de}$ plane: We examine the $\omega_{de} - \omega'_{de}$ plane, where ω'_{de} represents the rate of change of the EoS parameter ω_{de} with respect to $\ln(a(t))$ [69]. It has also been found that the $\omega_{de} - \omega'_{de}$ plane can be split into two regions: thawing ($\omega_{de} < 0$, $\omega'_{de} > 0$) and freezing ($\omega_{de} < 0$, $\omega'_{de} < 0$). The freezing region corresponds to a phase of faster cosmic acceleration compared to the thawing region.

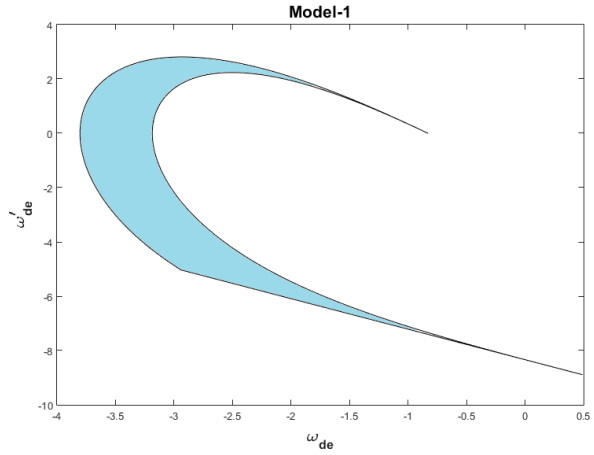

Figure 13. Plot of $\omega_{de} - \omega'_{de}$ plane for model-1.

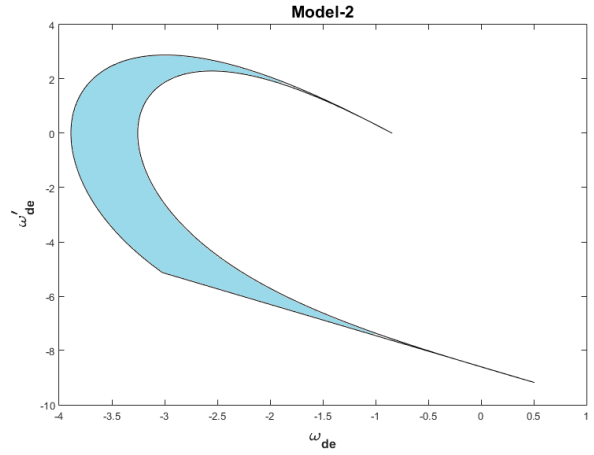

Figure 14. Plot of $\omega_{de} - \omega'_{de}$ plane for model-2.

Figs. 13 and 14 illustrate the trajectories of the BHDE models in the $\omega_{de} - \omega'_{de}$ phase plane. The shaded regions correspond to the 1σ confidence band for the parameter $b_4 = -0.091^{+0.013}_{-0.012}$. This diagnostic plane is especially useful in classifying DE models into thawing and freezing behaviours. Thawing region is defined by ($\omega_{de} < 0$, $\omega'_{de} > 0$), thawing models describe DE that was initially frozen at $\omega_{de} \simeq -1$ (cosmological constant–like) and then evolves towards less negative values. This regime typically corresponds to slower acceleration and a late-time deviation from ΛCDM. Freezing region is defined by ($\omega_{de} < 0$, $\omega'_{de} < 0$), freezing models evolve towards $\omega_{de} \to -1$, indicating a stronger tendency towards accelerated expansion. In this case, DE dynamics slow down asymptotically, producing a phase of more rapid cosmic acceleration compared to thawing models. Both model-1 (Hubble cutoff) and model-2 (GO cutoff) predominantly lie in the freezing region, as indicated by $\omega_{de} < 0$ and $\omega'_{de} < 0$ over most of the evolution. This suggests that the BHDE framework naturally drives the Universe towards a phase of faster acceleration at late times. The parameter $b_4 < 0$ ensures that ω_{de} remains deeply in the phantom regime ($\omega_{de} < -1$) for substantial intervals, while ω'_{de} is negative, reinforcing the freezing behaviour. The narrow shaded band implies that this classification is stable against 1σ variations in b_4. Both models show a qualitatively similar trajectory in the $\omega_{de} - \omega'_{de}$ plane. However, Model-2 (GO cutoff) produces a slightly less steep descent in ω'_{de}, which suggests a milder approach to the freezing regime compared to Model-1. This aligns with earlier findings that the GO cutoff yields more moderate dynamical behaviour and is closer to observationally preferred values. The freezing behaviour in both models is consistent with a late-time Universe dominated by a phantom-like DE component, driving accelerated expansion more efficiently than ΛCDM.

Squared sound speed: The squared sound speed

$$v_s^2 = \frac{\dot{p}_{de}}{\dot{\rho}_{de}} = \omega_{de} + \frac{\rho_{de}}{\dot{\rho}_{de}}\,\dot{\omega}_{de}. \tag{36}$$

is a primary diagnostic for the classical (linear) stability of cosmic fluids and effective DE components. If $v_s^2 > 0$ small perturbations oscillate (or propagate), and the background is classically stable at the linear level. Conversely, $v_s^2 < 0$ implies exponentially growing modes and a classical instability of the effective fluid, signalling that the background solution is not robust under perturbations.

Figs. 15 and 16 show the behavior of $v_s^2(z)$ for model-1 and model-2. The shaded band corresponds to the 1σ variation induced by the parameter $b_4 = -0.091^{+0.013}_{-0.012}$, so the blue region indicates the uncertainty in the predicted v_s^2

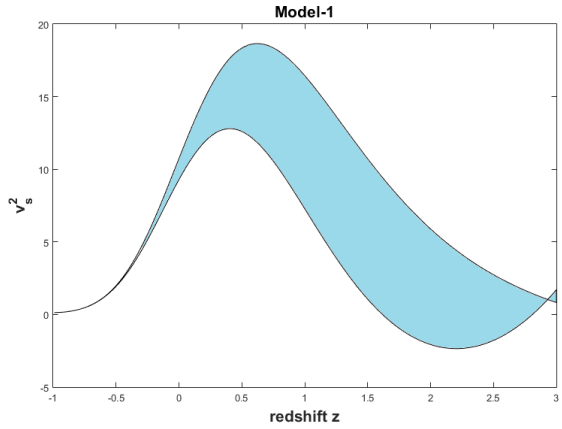

Figure 15. Plot of v_s^2 versus redshift for model-1.

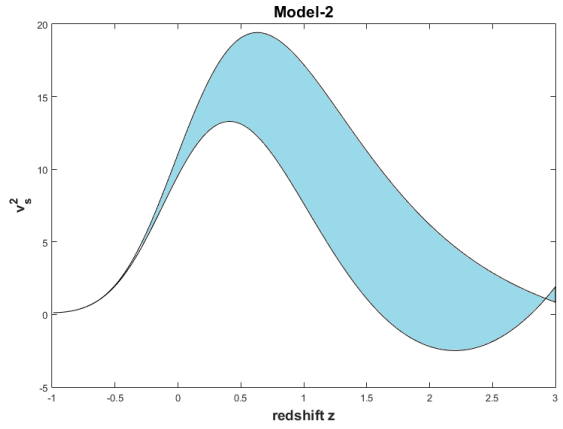

Figure 16. Plot of v_s^2 versus redshift for model-2.

due to the allowed range of b_4. For both models v_s^2 is positive over a substantial redshift interval (approximately around $0 \lesssim z \lesssim 2$ in the plots). This positive region indicates that — at least at the linear perturbation level — the models are classically stable during the recent cosmic history and around the epoch where DE dynamics is most relevant. At larger redshift (or at the far end of the plotted range) v_s^2 declines and in the displayed examples it approaches or crosses slightly below zero. Where v_s^2 becomes negative, the model develops a classical instability for perturbations in that epoch. The two models show qualitatively similar $v_s^2(z)$ shapes and uncertainty bands for the given b_4 range, although small quantitative differences are present in the peak height and the redshift where v_s^2 declines. Model-2 (GO cutoff) tends to produce a slightly more moderate peak and a somewhat narrower band at intermediate z, consistent with earlier findings that the GO cutoff yields milder departures from ΛCDM for comparable parameters. Both models, however, share the same qualitative features: a stable positive region followed by a decline and potential instability at larger $|z|$.

5. CONCLUSIONS

In this work, we have constructed anisotropic BT-*II* cosmological models within the framework of Self-creation theory of gravitation, considering BHDE with two different IR cutoffs: the Hubble horizon and the GO cutoff. By assuming a suitable relation between metric potentials, we obtained exact solutions of the field equations and explored the dynamical and observational features of the models. The main conclusions can be summarized as follows:

- The contour plot obtained from Hubble CC data, which provides joint constraints on the model parameter b_4 and the present Hubble constant H_0. The analysis yields the best-fit values $b_4 = -0.091^{+0.013}_{-0.012}$, $H_0 = 72.3 \pm 2.7$ km s^{-1}Mpc^{-1}. The contour plots confirm the robustness of these constraints, while the $H(z)$ fit demonstrates consistency with the observed expansion history and mild deviations from ΛCDM at high redshifts.

- The scalar field $\phi(z)$ decreases monotonically with evolution of the models, with larger values at higher redshift indicating its strong dynamical contribution in the early Universe. At low z, the scalar field contribution diminishes, consistent with a DE-dominated accelerated phase. The models successfully reproduce the transition from a past decelerated epoch ($q > 0$) to the present accelerating epoch ($q < 0$). The transition redshift lies in the interval $z_{tr} \sim$ 0.6–0.8, which is in excellent agreement with observational estimates from SNeIa and BAO data [70, 71]. In the (r, s) plane, both models evolve away from the ΛCDM fixed point $(r, s) = (1, 0)$, entering regions corresponding to quintessence and phantom behaviour depending on epoch. In the (r, q) plane, the trajectories clearly demonstrate the transition from the SCDM point $(1, 0.5)$ (matter-dominated decelerated era) to the de-Sitter model $(1, -1)$ (cosmological constant-dominated accelerated era).

- The deviation parameter γ shows strong growth around the transition epoch ($z \sim$ 1–2), signaling maximum deviations from isotropy and enhanced dynamical effects of DE. At late times, $\gamma \to 0$, restoring isotropy and a ΛCDM-like state. Model-2 again demonstrates a more stable and narrower evolution of γ compared to model-1, suggesting that anisotropic effects are better regulated under the GO cutoff. The WEC and NEC are largely satisfied in both models. However, the SEC is violated in the low-redshift regime, which is consistent with the requirement for cosmic acceleration. The DEC is upheld in most cases, validating the physical viability of the models.

- Both models exhibit a quintom-like behaviour, evolving across the cosmological constant boundary $\omega_{de} = -1$. At low redshift, ω_{de} remains close to -1, consistent with current Planck 2018 bounds [72] ($\omega_{de} = -1.03 \pm 0.03$), while at higher redshifts both models transition into the phantom regime ($\omega_{de} < -1$). The shaded regions confirm that this transition is robust under observational uncertainties. Both models lie predominantly in the freezing region ($\omega_{de} <$

Table 1. Comparison of cosmological behaviour between Model-1 (Barrow HDE with Hubble cutoff) and Model-2 (Barrow HDE with GO cutoff).

Diagnostic	**Model-1 (Hubble cutoff)**	**Model-2 (GO cutoff)**
Scalar field $\phi(z)$	Monotonically increasing with redshift and slightly stronger growth	Same behavior as model-1
Deceleration parameter $q(z)$	Clear transition at $z_{tr} \sim 0.6$–0.8 consistent with data	Same behavior as model-1
Statefinder (r, s) **plane**	Model finally approaches to ΛCDM $(1, 0)$ model and also shows quintessence and phantom phases	Same behavior as model-1
(r, q) **plane**	Transition from SCDM $(1, 0.5)$ to de-Sitter $(1, -1)$ and larger spread	Same transition as model-1
Energy conditions	WEC and NEC satisfied, SEC violated at late times (required for acceleration) and DEC valid mostly	Similar behaviour but with fewer violations and more consistent with cosmic acceleration
Skewness parameter γ	Peaks strongly around $z \sim 1-2$, larger deviations from isotropy and broader band	Similar peak but narrower confidence region and anisotropy effects better controlled
Equation of state parameter ω_{de}	Shows quintom behaviour, crosses $\omega = -1$ and broader uncertainty band	Similar quintom behaviour, smoother trajectory and closer to Planck constraints
$\omega_{de} - \omega'_{de}$ **plane**	Mostly in freezing region and strong acceleration phase	Also in freezing region and smoother evolution but closer to de-Sitter attractor
Squared sound speed v_s^2	Stability at intermediate z, instabilities at certain epochs and wider uncertainty	More stable evolution, reduced instabilities and narrower uncertainty band

$0, \omega'_{de} < 0$), corresponding to stronger cosmic acceleration compared to thawing models. This indicates that the DE dynamics in these models naturally drive a future de Sitter-like phase. The squared sound speed v_s^2 exhibits both positive and negative values. In the intermediate redshift regime, $v_s^2 > 0$ confirms stability, while instabilities ($v_s^2 < 0$) arise at certain epochs. Model-2 provides a smoother and more stable profile compared to model-1, with narrower uncertainty bands, suggesting that the GO cutoff yields a more observationally consistent description.

Finally, both BHDE models (Hubble and GO cutoffs) are consistent with observational constraints and reproduce the main features of cosmic evolution, including the transition from deceleration to acceleration, quintom behaviour of DE, and late-time convergence to ΛCDM-like dynamics. Model-1 (Hubble cutoff) shows slightly stronger deviations and broader uncertainty bands, while model-2 (GO cutoff) provides smoother trajectories, reduced anisotropies, and better stability properties. This suggests that the GO cutoff may represent a more robust framework for describing the late-time dynamics of the Universe.

Acknowledgment: We thank the reviewers/editor for their constructive comments which have considerably improved the presentation of our work. Y. Aditya expresses gratitude to the National Board for Higher Mathematics, Department of Atomic Energy, Government of India, for their financial support under grant No: 02011/8/2023 NBHM(R.P.)/R & D II/3073.

ORCID

U.Y. Divya Prasanthi, https://orcid.org/0009-0004-5397-050X; **D. Tejeswararao**, https://orcid.org/0000-0003-3508-346X; **Diddi Srinivasa Rao**, https://orcid.org/0009-0001-6890-9603; **Y. Aditya**, https://orcid.org/0000-0002-5468-9697; **D. Ram Babu**, https://orcid.org/0009-0008-7791-5977

REFERENCES

[1] S. Perlmutter, et al., Astrophys. J. **517**, 565 (1999). https://doi.org/10.1086/307221

[2] A. G. Riess, et al., Astron. Soc. Pac. **112**, 1284 (2000). https://doi.org/10.1086/316624

[3] M. Tegmark, et al., Phys. Rev. D, **69**, 103501 (2004). https://doi.org/10.1103/PhysRevD.69.103501
[4] L. Susskind, J. Math. Phys. **36**, 6377 (1994). http://dx.doi.org/10.1063/1.531249
[5] R. Bousso, JHEP, **07**, 004 (1999). https://doi.org/10.1088/1126-6708/1999/07/004
[6] A. Cohen, et al., Phys. Rev. Lett. **82**, 4971 (1999). https://doi.org/10.1103/PhysRevLett.82.4971
[7] M. Tavayef, et al., Phys. Lett. B, **781**, 195 (2018). https://doi.org/10.1016/j.physletb.2018.04.001
[8] C. Tsallis, and L.J.L. Cirto, Eur. Phys. J. C, **73**, 2487 (2013). https://doi.org/10.1140/epjc/s10052-013-2487-6
[9] A.S. Jahromi et al., Phys. Lett. B, **780**, 21 (2018). https://doi.org/10.1016/j.physletb.2018.02.052
[10] H. Moradpour et al., Eur. Phys. J. C, **78**, 829 (2018). https://doi.org/10.1140/epjc/s10052-018-6309-8
[11] Y. Aditya, and D.R.K. Reddy, Eur. Phys. J. C, **78**, 619 (2018). https://doi.org/10.1140/epjc/s10052-018-6074-8
[12] Y. Aditya, and D.R.K. Reddy, Astrophys. Space Sci. **363**, 207 (2018). https://doi.org/10.1007/s10509-018-3429-4
[13] U.Y. Divya Prasanthi, and Y. Aditya, Results Phys. **17**, 103101 (2020). https://doi.org/10.1016/j.rinp.2020.103101
[14] Y. Aditya, Bulgarian Astronomical Journal **40**, 95 (2024). https://astro.bas.bg/AIJ/issues/n40/YAditya.pdf
[15] Y. Aditya, and U.Y.D. Prasanthi, Bulgarian Astronomical Journal **38**, 52 (2023). https://astro.bas.bg/AIJ/issues/n38/YAditya.pdf
[16] Y. Aditya, et al., East Eur. J. Phys. **1**, 85 (2024). https://doi.org/10.26565/2312-4334-2024-1-06
[17] A. V. Prasanthi, et al., East Eur. J. Phys. **2**, 10 (2024). https://doi.org/10.26565/2312-4334-2024-2-01
[18] V.U.M. Rao, et al., Results in Physics, **10**, 469 (2018). https://doi.org/10.1016/j.rinp.2018.06.027
[19] M.V. Santhi, et al., Int. J. Theor. Phys. **56**, 362 (2017). https://doi.org/10.1007/s10773-016-3175-8
[20] Y. Aditya, et al., Eur. Phys. J. C, **79**, 1020 (2019). https://doi.org/10.1140/epjc/s10052-019-7534-5
[21] A. Iqbal, and A. Jawad, Physics of the Dark Universe, **26**, 100349 (2019). https://doi.org/10.1016/j.dark.2019.100349
[22] G. Kaniadakis, Physica A: Stat. Mech. and its Appl. **296**(3-4), 405 (2001). https://doi.org/10.1016/S0378-4371(01)00184-4
[23] M. Masi, Phys. Lett. A, **338**, 217 (2005). https://doi.org/10.1016/j.physleta.2005.01.094
[24] E.M. Abreu, et al., EPL (Europhysics Letters), **124**, 30003 (2018). https://doi.org/10.1209/0295-5075/124/30003
[25] J. D. Barrow, S. Basilakos, and E. N. Saridakis, Phys. Lett. B, **815**, 136134 (2021). https://doi.org/10.1016/j.physletb.2021.136134
[26] G. G. Luciano, and E. N. Saridakis, Eur. Phys. J. C, **82**, 558 (2022). https://doi.org/10.1140/epjc/s10052-022-10530-7
[27] G. G. Luciano, Phys. Rev. D, **106**, 083530 (2022). https://doi.org/10.1103/PhysRevD.106.083530
[28] A. Oliveros, et al., Eur. Phys. J. Plus. **137**, 783 (2022). https://doi.org/10.1140/epjp/s13360-022-02994-z
[29] A. Remya, et al., Int. J. Geom. Methods Mod. Phys. **19**, 2250082 (2022). https://doi.org/10.1142/S0219887822500827
[30] M. Koussour, et al., Int. J. Mod. Phys. A, **37**, 2250184 (2022). https://doi.org/10.1142/S0217751X22501846
[31] Y. Aditya, et al., Afrika Matematika, **36**, 120 (2025). https://doi.org/10.1007/s13370-025-01340-7
[32] G.A. Barber, Gen. Relativ. Gravit. **14**, 117 (1982). https://doi.org/10.1007/BF00756918
[33] T. Singh, Astrophys. Space Sci. **102**, 67 (1984). https://doi.org/10.1007/BF00651062
[34] D.R.K. Reddy, Astrophys. Space Sci. **133**, 389 (1987). https://doi.org/10.1007/BF00642496
[35] V.U.M. Rao, et al., Astrophys Space Sci. **317**, 83 (2008). https://doi.org/10.1007/s10509-008-9859-7
[36] R.L. Naidu, et al., Astrophys Space Sci. **358**, 23 (2015). https://doi.org/10.1007/s10509-015-2421-5
[37] V.U.M. Rao, and U.Y.D. Prasanthi, Can. J. Phys. **95(6)**, 554 (2017). https://doi.org/10.1139/cjp-2017-0014
[38] R.R. Caldwell, and M. Kamionkowski, Ann. Rev. Nucl. Part. Sci. **59**, 397 (2009). https://doi.org/10.1146/annurev-nucl-010709-151330
[39] K. Bamba, et al., Astrophys. Space Sci. **342**, 155 (2012). https://doi.org/10.1007/s10509-012-1181-8
[40] S. Nojiri, et al., Phys. Rept. **692**, 1 (2017). https://doi.org/10.1016/j.physrep.2017.06.001
[41] Y. Aditya, D.R.K. Reddy, Eur. Phys. J. C, **78**, 619 (2018). https://doi.org/10.1140/epjc/s10052-018-6074-8
[42] V.U.M. Rao, et al., Results in Physics, **10**, 469 (2018). https://doi.org/10.1016/j.rinp.2018.06.027
[43] Y. Aditya, et al., Eur. Phys. J. C, **79**, 1020 (2019). vhttps://doi.org/10.1140/epjc/s10052-019-7534-5
[44] U.K. Sharma, et al., IJMPD, **31**, 2250013 (2022). https://doi.org/10.1142/S0218271822500134
[45] U.Y.D. Prasanthi, and Y. Aditya, Results of Physics, **17**, 103101 (2020). https://doi.org/10.1016/j.rinp.2020.103101
[46] U.Y.D. Prasanthi, and Y. Aditya, Physics of the dark universe, **31**, 100782 (2021). https://doi.org/10.1016/j.dark.2021.100782
[47] Y. Aditya, D.R.K. Reddy, Astrophys. Space Sci, **363**, 207 (2018). https://doi.org/10.1007/s10509-018-3429-4
[48] Y Aditya, et al., Results in Physics, **12**, 339 (2019). https://doi.org/10.1016/j.rinp.2018.11.074
[49] Y. Aditya, et al. Astrophys. Space Sci. **364**, 190 (2019). https://doi.org/10.1007/s10509-019-3681-2
[50] Y. Aditya, et al., Int. J. Mod. Phys. A, **37**, 2250107 (2022). https://doi.org/10.1142/S0217751X2250107X

[51] A. Jawad, et al. Symmetry, **10**, 635 (2018). https://doi.org/10.3390/sym10110635
[52] C.B. Collins, et al., Gen. Relativ. Gravit. **12**, 805 (1980). https://doi.org/10.1007/BF00763057
[53] K.S. Thorne, Astrophys. J. **148**, 51 (1967). https://doi.org/10.1086/149127
[54] R. Kantowski, and R.K. Sachs, J. Math. Phys. **7**, 433 (1966). https://doi.org/10.1063/1.1704952
[55] J. Kristian, and R.K. Sachs, Astrophys. J. **143**, 379 (1966). http://dx.doi.org/10.1086/148522
[56] V.B. Johri, and R. Sudharsan, Australian Journal of Physics, **42(2)**, 215 (1989). https://doi.org/10.1071/PH890215
[57] V.B. Johri, and K. Desikan, Gen. Relat. Gravit. **26**, 1217 (1994). https://doi.org/10.1007/BF02106714
[58] K. D. Raju, et al., Astrophys. Space Sci. **365**, 28 (2020). https://doi.org/10.1007/s10509-020-3729-3
[59] K. D. Raju, et al., Astrophys. Space Sci. **365**, 45 (2020). https://doi.org/10.1007/s10509-020-03753-1
[60] Y. Aditya, et al., Indian J. Phys. **95**, 383 (2021). https://doi.org/10.1007/s12648-020-01722-6
[61] K.D. Naidu, et al., Int. J. Mod. Phys. A, **36**(8), 2150054 (2021). https://doi.org/10.1142/S0217732321500541
[62] R.L. Naidu, et al., New Astron. **85**, 101564 (2021). https://doi.org/10.1016/j.newast.2020.101564
[63] Y. Aditya, Bulg. Astron. J. **39**, 12 (2023). https://astro.bas.bg/AIJ/issues/n39/YAditya.pdf
[64] L. N. Granda, and A. Oliveros, Phys. Lett. B, **669**, 275 (2008). https://doi.org/10.1016/j.physletb.2008.10.017
[65] L. N. Granda, and A. Oliveros, Phys. Lett. B, **671**, 199 (2009). https://doi.org/10.1016/j.physletb.2008.12.025
[66] J. Simon, L. Verde, and R. Jimenez, Phys. Rev. D, **71**, 123001 (2005). https://doi.org/10.1103/PhysRevD.71.123001
[67] G.S. Sharov, and V.O. Vasiliev, Math. Model. Geom. **6**, 1-20 (2018).
[68] V. Sahni, et al. J. Exp. Theor. Phys. Lett. **77**, 201 (2003). https://doi.org/10.1134/1.1574831
[69] R. Caldwell, and E.V. Linder, Phys. Rev. Lett. **95**, 141301 (2005). https://doi.org/10.1103/PhysRevLett.95.141301
[70] S. Capozziello, et al., MNRAS, **484**, 4484 (2019). https://doi.org/10.1093/mnras/stz176
[71] G. F. Hinshaw, et al., Astrophys. J. Suppl. **208**, 19 (2018). https://doi.org/10.1088/0067-0049/208/2/19
[72] N. Aghanim, et al., A&A **641**, A6 (2020). https://doi.org/10.1051/0004-6361/201833910

КОСМОЛОГІЧНА ДІАГНОСТИКА ГОЛОГРАФІЧНОЇ ТЕМНОЇ ЕНЕРГІЇ ВСЕСВІТУ БАРРОУ ТИПУ БІАНКІ-II

У.Й. Дів'я Прасанті[1], **Д. Техесварарао**[2], **Дідді Шрініваса Рао**[3], **Ю. Адітья**[4], **Д. Рам Бабу**[4]

[1]*Департамент статистики & математики Коледж садівництва, доктор Y.S.R. Садівничий університет, Парватіпурам-535502, Індія*

[2]*Кафедра фундаментальних та гуманітарних наук, Технологічний інститут GMR (GMRIT) – вважається університетом, Раджам-532127, Індія*

[3]*Кафедра математики, Університет Адітья, Сурампалем-533437, Індія*

[4]*Кафедра математики, Технологічний інститут GMR (GMRIT) – вважається університетом, Раджам-532127, Індія*

У цій статті ми досліджуємо анізотропну космологічну модель типу *II* Біанкі в рамках голографічної темної енергії Барроу, розглядаючи як горизонт Хаббла, так і шкалу Гранда–Оліверoса як інфрачервоні обрізання. Щоб отримати точні розв'язки рівнянь поля Ейнштейна, ми припускаємо відповідне співвідношення між метричними потенціалами. Використовуючи дані космічного хронометра Хаббла, ми обмежуємо параметри моделі та отримуємо значення найкращого наближення $b_4 = -0,091^{+0,013}_{-0,012}$ та $H_0 = 72,3 \pm 2,7$ км с$^{-1}$Мпк$^{-1}$. $H(z)$ апроксимація демонструє чудову відповідність з даними спостережень та перекриття з ΛCDM при низьких червоних зміщеннях, з незначними відхиленнями при вищих z. Фізичну поведінку моделі досліджують за допомогою детального аналізу космологічних параметрів. Параметр уповільнення $q(z)$ демонструє плавний перехід від ранньої фази уповільнення до сучасної епохи прискорення. Параметр рівняння стану ω_{de} демонструє квінтомоподібну динаміку, розвиваючись через межу космологічної константи та входячи у фантомний режим, що узгоджується з прискоренням наприкінці часу. Стабільність перевіряється за допомогою квадрата швидкості звуку v_s^2, який залишається додатним у нещодавньому Всесвіті, що забезпечує класичну стабільність. Фазова площина $\omega_{de} - \omega'_{de}$ вказує на те, що обидві моделі лежать в області замерзання, що відповідає швидшому прискоренню. Діагностика стану (r, s) та (r, q) додатково підтверджує перехід від стандартної фази, де домінує холодна темна матерія, до атрактора, подібного до де Ситтера, з траєкторіями, що показують чіткі відхилення від ΛCDM.

Ключові слова: *модель Біанкі типу II; голографічна темна енергія Барроу; темна енергія; космологія; модифікована теорія гравітації*